Latitudinal variation in methane abundance above clouds in Neptune's atmosphere from VLT/MUSE-NFM: Limb-darkening reanalysis

Patrick G. J. Irwin[1], Jack Dobinson[1], Arjuna James[1], Daniel Toledo[2], Nicholas A. Teanby[3], Leigh N. Fletcher[4], Glenn S. Orton[5], Santiago Pérez-Hoyos[6]

[1]Department of Physics, University of Oxford, Parks Rd, Oxford, OX1 3PU, UK

[2]Daniel - Spain

[3]School of Earth Sciences, University of Bristol, Wills Memorial Building, Queens Road, Bristol, BS8 1RJ, UK

[4]Department of Physics & Astronomy, University of Leicester, University Road, Leicester, LE1 7RH, UK

[5]Jet Propulsion Laboratory, California Institute of Technology, 4800 Oak Grove Drive, Pasadena, CA 91109, USA

[6]Dpto. Física Aplicada I, ETSI, Universidad del País Vasco UPV/EHU, 48013 Bilbao, Spain

Key Points:

- Using Minnaert Limb-darkening analysis improves things enormously.

Corresponding author: Patrick Irwin, `patrick.irwin@physics.ox.ac.uk`

Abstract

Observations of Neptune, made in 2018 with the Multi Unit Spectroscopic Explorer (MUSE) instrument at the Very Large Telescope (VLT) in Narrow Field Adaptive Optics mode (Irwin et al., Icarus, 311, 2019) have been reanalysed to incorporate the effects of limb-darkening. We present a new analysis technique, based upon the Minnaert limb-darkening approximation model that is found to provide much stronger constraint on the cloud structure and methane abundance, makes better use of the available data and is also more computationally efficient. We find a very similar variation in cloud-top methane abundance as previously reported, but with much better constraint.

Plain Language Summary

Minnaert good.

1 Introduction

The visible and near-infrared spectrum of Neptune is formed by the reflection of sunlight from the atmosphere modulated mostly by the absorption of gaseous methane. The measured spectra can thus be inverted to determine the cloud structure as a function of location and altitude providing we know the vertical and latitudinal distribution of methane. Although for some years the vertical profiles of methane as determined from Voyager 2 radio-occultation observations were used at all latitudes, HST/STIS observations of Uranus recorded in 2002 (Karkoschka & Tomasko, 2009) and similar observations of Neptune recorded in 2003 (Karkoschka & Tomasko, 2011) both showed the methane abundance to vary significantly with latitude on both planets. These HST/STIS observations utilised the collision-induced absorption (CIA) bands of H_2–H_2 and H_2–He near 825 nm which allow variations of CH_4 abundance to be differentiated from cloud-top pressure variations. Karkoschka and Tomasko (2009, 2011) found that the methane abundance near the main observable H_2S cloud tops at 2–3 bar varies from $\sim 4\%$ at equatorial latitudes to $\sim 2\%$ at polar latitudes for both planets.

More recently, and analysis of VLT/MUSE observations (Irwin et al., 2019) found a similar latitudinal variation of cloud-top methane abundance in Neptune's atmosphere, varying from 4–5% at equatorial latitudes reducing to 3–4% at polar latitudes. In this paper,

we reanalyse these data using a new limb-darkening approximation model, which we find considerably improves our determined methane abundances.

2 MUSE Observations

3 Analysis

3.1 Limb-darkening analysis

The dependence of the observed reflectivity from a location on a planet on the incidence and emission angles can be well approximated using an empirical law first introduced by Minnaert (1941), and which and was recently applied to Jupiter observations by Pérez-Hoyos et al. (2020). For an observation at a particular wavelength, the observed reflectivity I/F can be approximated as:

$$\frac{I}{F} = \left(\frac{I}{F}\right)_0 \mu_0^k \mu^{k-1} \tag{1}$$

where $(I/F)_0$ is the nadir-viewing reflectivity, k is the limb-darkening parameter, and μ and μ_0 are, respectively, the cosines of the emission and solar incidence angles. With this model a value of $k = 0.5$ indicates Lambertian scattering, $k > 0.5$ indicates limb-darkening, while $k < 0.5$ indicates limb-brightening. Taking logarithms of both sides, Eq. 1 can be re-expressed as:

$$\ln\left(\mu\frac{I}{F}\right) = \ln\left(\frac{I}{F}\right)_0 + k\ln(\mu\mu_0) \tag{2}$$

and we can see that it is possible to fit the Minnaert parameters $(I/F)_0$ and k if we perform a least-squares fit on a set of measurements of $\ln(\mu I/F)$ as a function of $\ln(\mu\mu_0)$.

We analysed the same 'cube' of Neptune as was studied by Irwin et al. (2019), namely 'Observation 3', recorded by VLT/MUSE at 09:43:21(UT) on 19th June 2019. We analysed the spectra in this cube in the wavelength range $800 - 900$ nm and Fig. 1 shows the observed appearance of the planet at 830 and 840 nm, which are wavelengths of weak and strong methane absorption respectively. The limb-darkening behaviour of the observed spectra were analysed in latitude bands of width $10°$, spaced every $5°$. For each band, the observed reflectivities were used to construct plots of $\ln(\mu I/F)$ against $\ln(\mu\mu_0)$ and straight lines fitted to deduce $(I/F)_0$ and k for each wavelength. Locations on the disc where there were
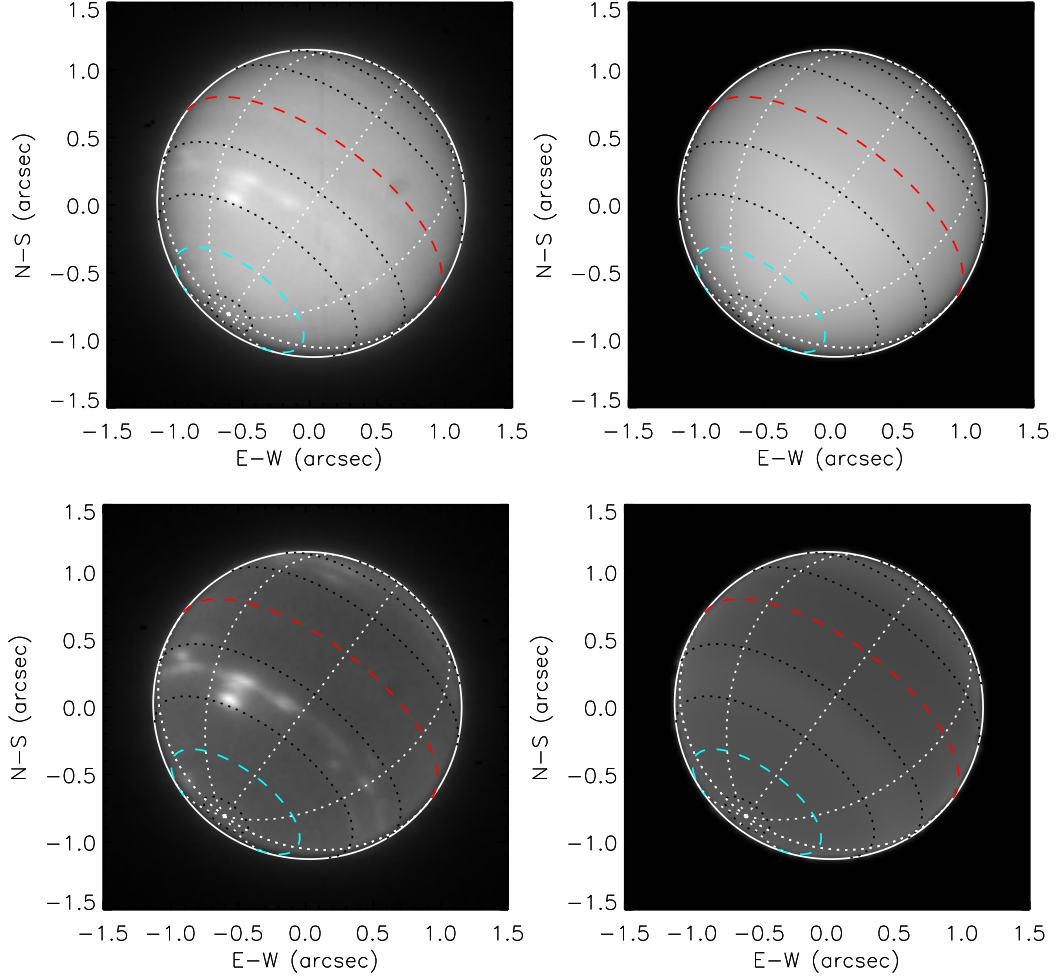
Figure 1. Appearance of Neptune on June 19th 2008 at 09:43:21UT (Observation '3' of Irwin et al. (2019)) at 830 nm (top row) and 840 nm (bottom row). The left-hand column shows the observed image, while the right-hand column shows the images reconstructed following a Minnaert limb-darkening analysis. The equator and 60°S latitude circles are indicated by the red-dashed and cyan-dashed lines, respectively.

bright clouds were masked out. Examples of these fits for 830 and 840 nm and for latitude bands centred on the equator and 60°S are shown in Fig. 2. Here it can be seen that Minnaert empirical law provides a very accurate approximation of the observed dependance of reflectivity with viewing zenith angles. Although all the measurements are plotted, only those measurements with $\mu\mu_0 >= 0.09$ (i.e., $\mu >\sim 0.3$) were used to fit $(I/F)_0$ and k to make sure that the fitting procedure is not overly affected by points measured near the disc edge (and thus more potentially more 'mixed' with space). Extending this analysis to all wavelengths under consideration, Fig. 3 shows a contour plot of the fitted values of $(I/F)_0$ and k for all wavelengths and latitude bands. It can be seen that at wavelengths near 830 nm, the fitted k values are greater than 0.5, indicating limb darkening, while at longer wavelengths, values of k less than 0.5 are fitted, indicating limb brightening. It can also just be seen in Fig. 3 that width of the reflectance peak of $(I/F)_0$ is noticably wider at latitides southward of $20 - 40°$S, a trend which is also just discernible in the fitted k values near the peak, indicating that the transition from limb-brightening to limb-darkening behaviour occurs is widened.

Having fitted values of $(I/F)_0$ and k for all wavelengths and latitude bands, it is then possible to reconstruct the apparent image of the planet at any observation geometry. Using the measured observation values of μ and μ_0 we reconstructed the fitted image of Neptune and 830 and 840 nm as seen by MUSE in Fig. 1. As can be seen the observed general dependence of reflectivity with latitude and position is well reproduced compared with the original MUSE observations.

3.2 Retrieval model

Having applied the Minnaert model to the observations we then used the fitted $(I/F)_0$ and k parameters to reconstruct synthetic spectra of Neptune for all the latitude bands concerned and used these as synthetic 'observations' to be fitted with our radiative transfer and retrieval model, NEMESIS (Irwin et al., 2008). There are two main advantages in doing this: 1) the spectra reconstructed using the fitted Minnaert parameters have smaller random error values as they have been reconstructed from values fitted to a combination of all the points in a latitude band; and 2) we can reconstruct the apparent spectrum of Neptune at any set of angles that is convenient for modelling, which can greatly reduced computation time as compared to our previous approach where, because we did not assume to know the zenith angle dependence, we tried to fit simultaneously to observations at several different
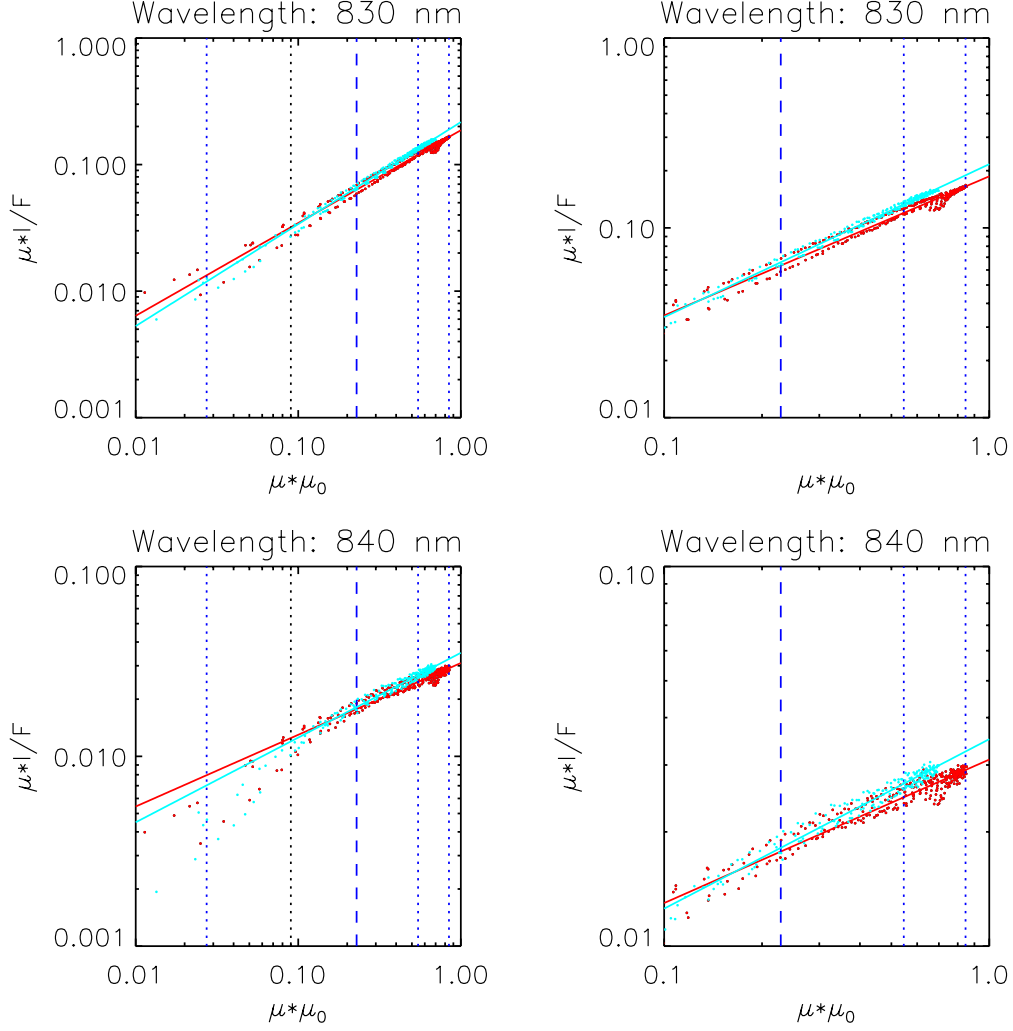
Figure 2. Minnaert analysis of observed limb-darkening curves at 830 nm (top row) and 840 nm (bottom row). The left-hand column shows all observations, while the right-hand column is limited to points with $\mu\mu_0 > 0.1$. The red points are the measurements at the equator, while those coloured cyan are at $60°$S. The vertical blue dotted lines indicate the values of $\mu\mu_0$ corresponding to our 5-point quadrature ordinates.
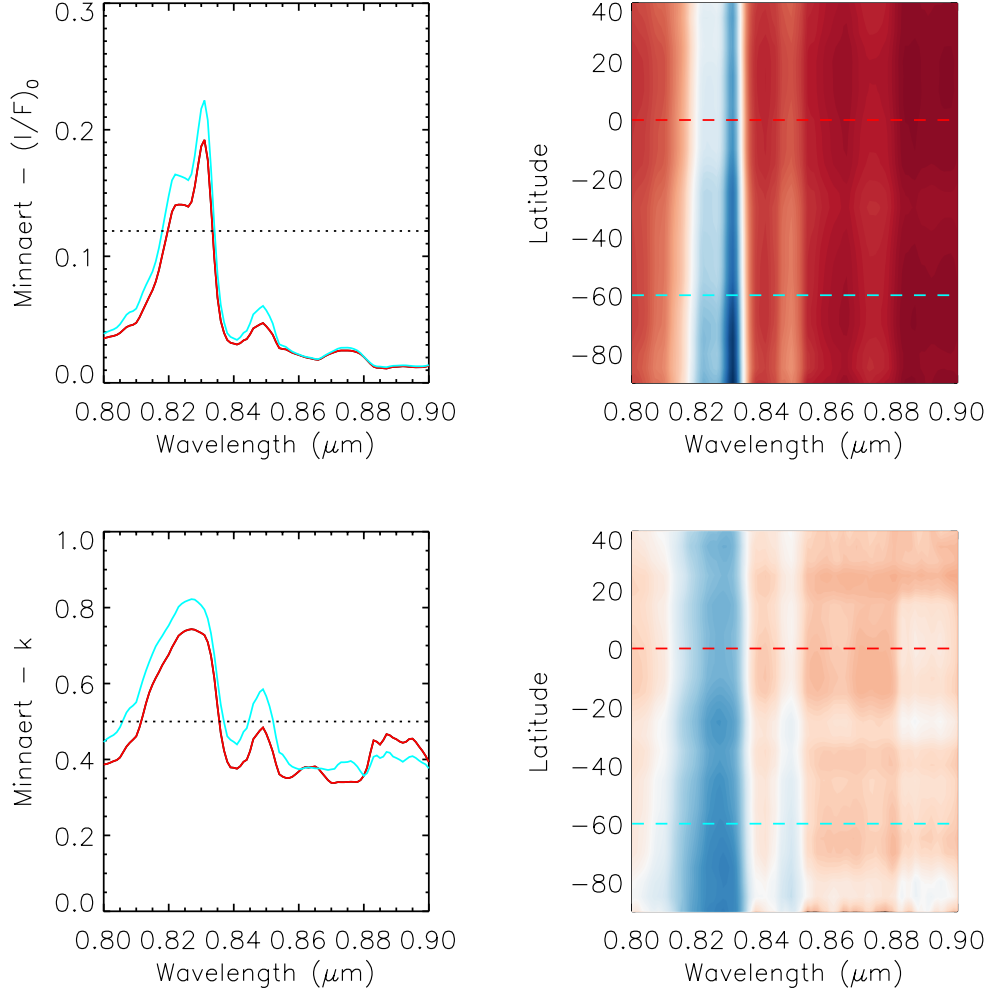
Figure 3. Minnaert analysis of observed limb-darkening curves from 800 to 900 nm and at all latitudes visible on Neptune's disc. The left-hand column shows the fitted values of $(I/F)_0$ and k at the equator (red) and 60°S (cyan), while the right-hand column shows a contour plot of these fitted parameters at all latitudes. The horizontal lines in the left hand column indicates the value of the white colour in the contour plots, and for the k contour plot indicates the transition from limb darkening ($k > 0.5$) to limb-brightening ($k < 0.5$)

.

Table 1. Five-point Gauss-Lobatto Quadrature Scheme used in this study

Index	μ	θ (°)	Weight
1	0.165278957666387	80.4866	0.327539761183898
2	0.477924949810444	61.4500	0.292042683679684
3	0.738773865105505	42.3729	0.224889342063117
4	0.919533908166459	23.1420	0.133305990851069
5	1.00000000000000	0.00000	0.022222222222222

zenith angles. For modelling the near-infrared reflectivity observations, NEMESIS employs a plane-parallel Matrix Operator multiple-scattering model (Plass et al., 1973). In this model, integration over zenith angle is done with a Gauss-Lobatto quadrature scheme, while the azimuth integration is done with Fourier decomposition. For most calculations, not too near to the disc edge, we have found that five zenith angles are usually sufficient and the reflectivity at a particular zenith angle is linearly interpolated between calculations done at the two closest zenith angles. This has a number of disadvantages: 1) it requires two sets of calculations for each location; and 2) the linear interpolation can lead to interpolation errors at larger zenith angle; and 3) for points near the disc edge, the number of Fourier components needed to fully resolve the azimuth dependence increases, which can further greatly increase computation time. By reconstructing spectra using the fitted Minnaert $(I/F)_0$ and k parameters we can simulate spectra measured as if they exactly coincided with the angles in our quadrature scheme and also, if we assume the Minnaert approximation to be true and which has a linear dependence in logarithmic space we need only fit to the spectra at two angles, and can test how well the linear approximation applies in post-processing. Hence, in the retrievals presented here we reconstructed two spectra for each latitude band, reconstructed with viewing zenith angle θ_V, solar zenith angle θ_S, and azimuth angle ϕ values of (0°, 0°, 180°) and (θ_2, θ_2, 180°), respectively, with $\phi = 180°$ indicating back-scattering, and where $\theta_2 = 61.45°$ is the second zenith angle in our Gauss-Lobatto scheme (Table 1), sufficiently high to probe limb-darkening or limb-brightening, but not too high to need an excessive number of Fourier components. Then for each latitude band the two synthetic observations at 0° and 61.45° zenith angle were fitted simultaneously to determine the latitudinal dependence of cloud structure and methane abundance.
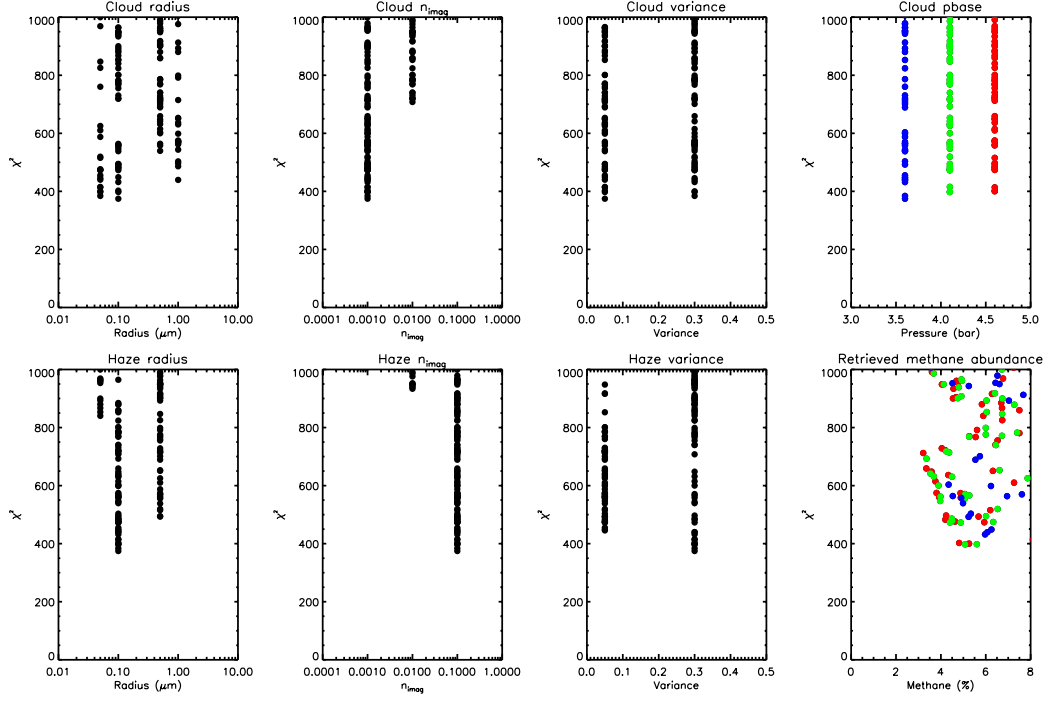
Figure 4. Variation of the goodness of fit of our retrievals (χ^2) in the equatorial band as a function of the assumed values of the grid point values defined in Table. 2.
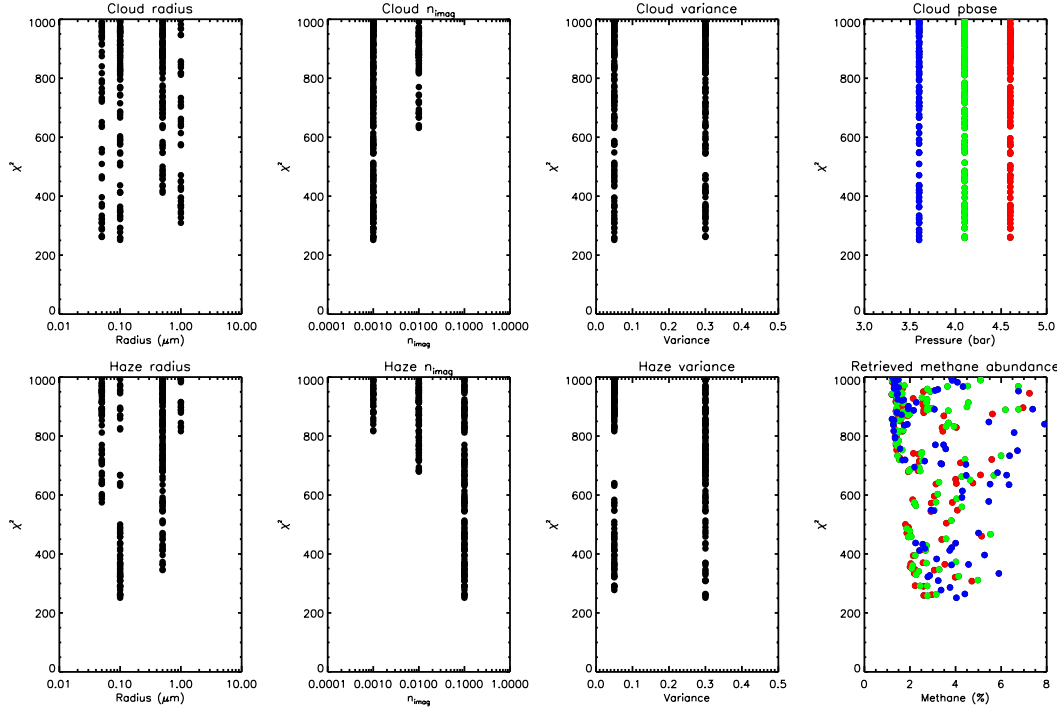

Figure 5. Variation of the goodness of fit of our retrievals (χ^2) in the band at $60°$S as a function of the assumed values of the grid point values defined in Table. 2.

As with our previous analysis (Irwin et al., 2019), we modelled the atmosphere of Neptune using 39 layers spaced equally (in log pressure) between ~ 10 and ~ 0.01 bar. We ran NEMESIS in correlated-k mode, and for methane absorption used a methane k-table generated from the band model Karkoschka and Tomasko (2010). The collision-induced absorption of H_2-H_2 and H_2-He near 825 nm was modelled with the coefficients of Borysow et al. (1989); Borysow and Frommhold (1989); Borysow et al. (2000), assuming a thermally-equilibriated ortho:para hydrogen ratio. Rayleigh scattering was included as described in Irwin et al. (2019) and the effects of polarization and Raman scattering were again justifiably ignored. Once again, we used the solar spectrum of (Chance & Kurucz, 2010), smoothed with a triangular line shape of FWHM $= 0.002 \, \mu$m and took Neptune's distance from the Sun on the date of observation to be 29.94 AU. The reference temperature and abundance profile is the same as that used by Irwin et al. (2019) and is based on the 'N' profile determined by Voyager-2 radio-occultation measurements (Lindal, 1992), with He:$H_2 = 0.177$ (15:85) including 0.3% mole fraction of N_2.

For clouds/hazes we again adopted the parameterised model used by (Irwin et al., 2016) to model VLT/SINFONI and Gemini/NIFS H-band observations of Neptune, and found to provide good limb-darkening/limb-brightening behaviour. Particles in the troposphere are modelled with a cloud with a variable base pressure (set to pressure of $\sim 3.6 - 4.6$ bar) and a scale height retrieved as a fraction of the pressure scale height, while scattering from haze particles is modelled with a second layer, with base pressure fixed at 0.03 bar and fixed fractional scale height of 0.1. The scattering properties of the cloud were calculated using Mie scattering and a retrievable imaginary refractive index spectrum with the real part of the refractive index constructed using a Kramers-Kronig analysis assuming $n_{real} = 1.4$ at 800 nm and approximating the phase function with combined Henyey-Greenstein functions.

3.3 Retrieval analysis

To best tune our retrieval model, we first concentrated on the latitude bands at the equator and 60°S. Fitting to just the $800 - 900$ nm region, we were aware from our previous study that there was likely to be a high degree of degeneracy in our best-fit solutions with respect to assumed particle sizes and other parameters. Hence, we first analysed these two latitude bands for a grid of preset values of cloud mean radius, variance of cloud radius distribution, cloud imaginary refractive index, haze mean radius, variance of haze radius distribution, haze imaginary refractive index, and cloud base pressure, described in Table 2.

Table 2. Parameter table

Parameter	Number	Values
Cloud radius mean	4	0.05, 0.1, 0.5, 1.0 μm
Cloud radius variance	3	0.05, 0.3
Cloud n_{imag}	3	0.001, 0.01, 0.1
Haze radius mean	4	0.05, 0.1, 0.5, 1.0 μm
Haze radius variance	3	0.05, 0.3
Haze n_{imag}	3	0.001, 0.01, 0.1
p_{base}	3	3.65, 4.15, 4.66 bar

From Table 2 we can see that the number of grid locations is $4 \times 3 \times 3 \times 4 \times 3 \times 3 \times 3 = 3888$ setups for each latitude band. For each set up we retrieved simultaneously four variables from the synthetic spectra reconstructed at $0°$ and $61.45°$ emission angle: 1) cloud opacity; 2) cloud fractional scale height; 3) haze opacity; and 4) the deep methane abundance. We assumed that the set imaginary refractive indices applied at all wavelengths simultaneously. After fitting we plotted the χ^2 of the fits as a function of the set grid parameters together with the retrieved methane cloud-top mole fraction, which we show in Fig. 4 for the equator and Fig. 5 for the 60°S latitude band. Here we can see that the goodness of fit and retrieved methane abundance depend little on the assumed deep pressure of the cloud, nor on the variance of the size distribution of the cloud and haze particles. However, we can see that there is a strong preference for solutions with a haze particle mean radius of $0.05 - 0.1$ μm and high imaginary refractive index of 0.1. For the cloud, it can be seen that the preference is for a low imaginary refractive index of 0.001. Retrievals where the cloud imaginary refractive index was set to 0.1 had χ^2 in excess of 1000 and so are not visible in Figs 4 and 5, but the constraint on the cloud mean radius is not strong, with values of $0.05 - 0.1$ μm slightly favoured over 1.0 μm. A cloud mean radius of 0.5 μm is not favoured. In addition, we checked to see if the limb-darkening curves modelled with our radiative transfer model at all zenith angles was consistent with the Minnaert law and found very good correspondence, adding confidence to our approach.
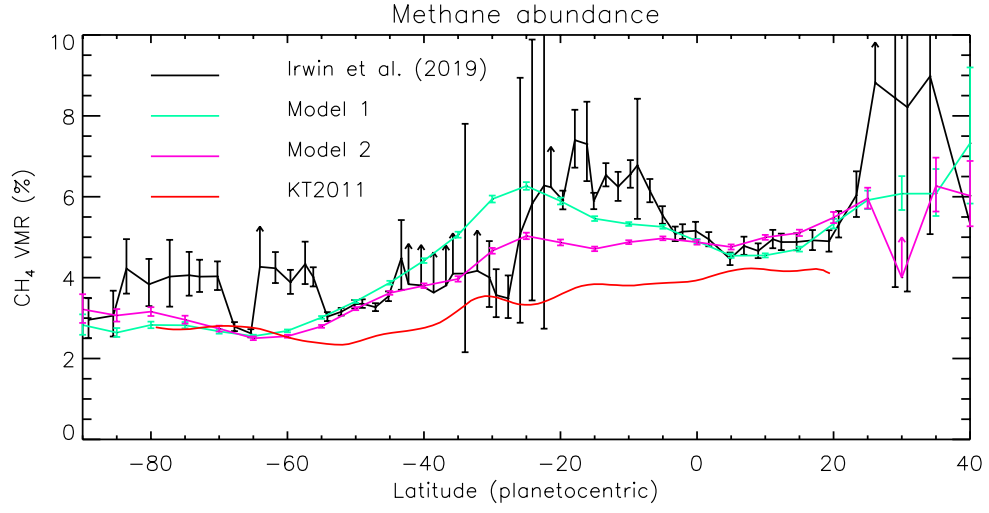
Figure 6. Fitted methane abundances as a function of latitude. The results from our previous work (Irwin et al., 2019) are shown for reference and compared with our new model: A) where the imaginary refractive indices of the haze and cloud are fixed to 0.1 and 0.001, respectively; and B) where the imaginary refractive indices of the haze and cloud are allowed to vary (keeping constant with wavelength). Also shown are the methane abundances estimated by (Karkoschka & Tomasko, 2011) (red), scaled to match our estimates. We see a clear decrease in methane abundance from $\sim 5\%$ at near-equatorial latitudes to $\sim 3\%$ polewards of 20–40°S.
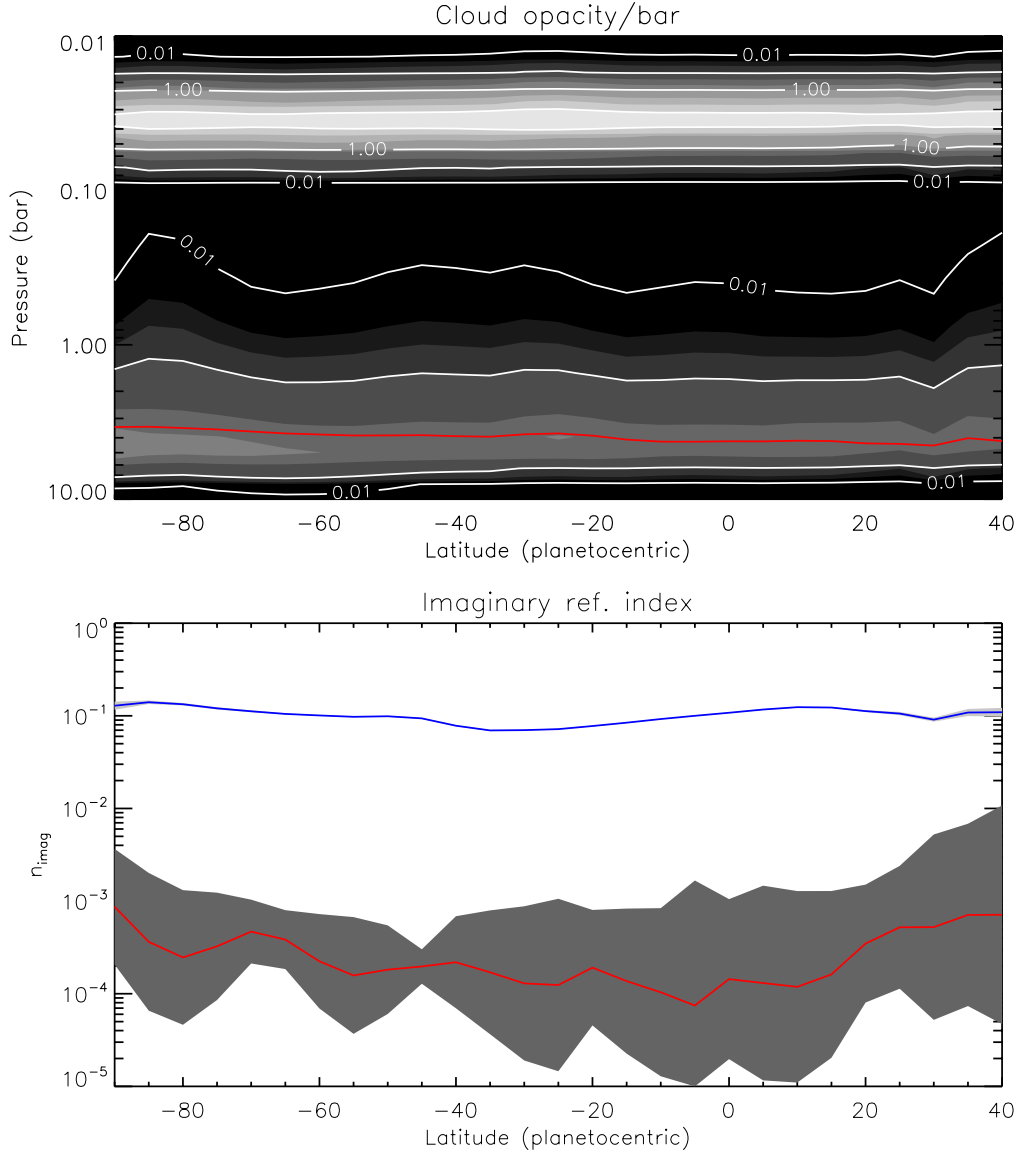
Figure 7. Fitted latitudinal variation of cloud opacity/bar (at 0.8 μm) and cloud/haze imaginary refractive indices. The top panel shows a contour plot of the fitted cloud opacity/bar profiles (brighter regions indicate greater cloud density). The bottom panel shows the latitudinal variation of the retrieved imaginary refractive indices of the cloud particles (red) and haze particles (blue), together with error range. The red line in the top plot indicates the cloud top pressure (i.e. level where overlying cloud opacity at 0.8 μm is unity). The cloud contour map indicates the main cloud top to lie at similar pressure levels at all latitudes and has a cloud-top pressure of ~ 4 bar. We can also see an increase in stratospheric haze at $20 - 40°$S, associated with the cloudy zone and then clearing towards the north and south.
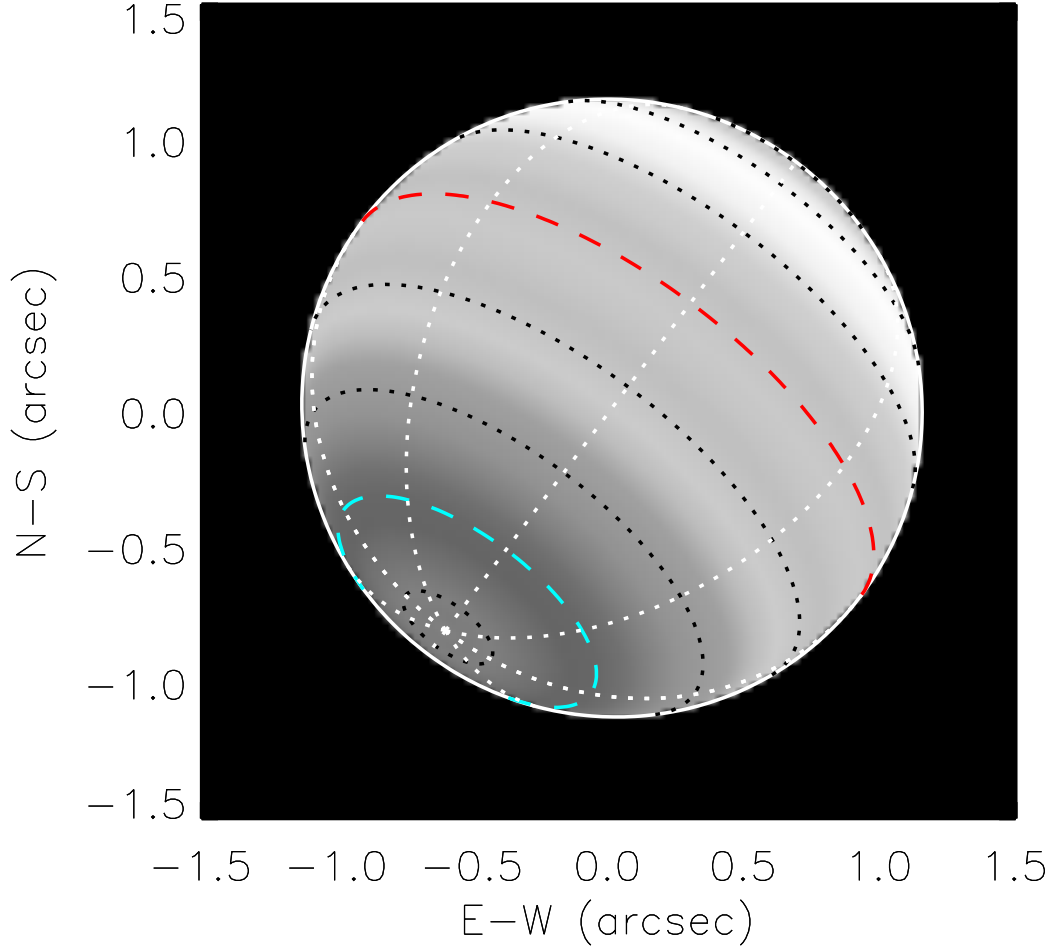
Figure 8. Fitted methane abundances (Model B) projected on to the Neptune's disc as seen by VLT/MUSE, showing clearly lower values polewards of 30°S and a possible local minimum at 60°S.

178   Although there are a wide range of best fit χ^2 values it is apparent that the best fits are

179   achieved for a methane abundance of $\sim 5 \pm 1$ at the equator and $\sim 3 \pm 1$ at 60°S. However,

180   although we clearly retrieve lower methane near the south pole than at the equator it is

181   clear that there are a wide range of possible cloud solutions that give equally poor fits to

182   the data but rather different methane abundance. Hence, although we can be fairly certain

183   that the polar methane cloud-top abundance is 0.6 (i.e., 3/5) times that at the equator, we

184   can be less certain of the absolute cloud-top methane abundances.

Having surveyed the range of cloud properties that best match the observed limb dark-ening at the equator and 60°S, we then took one of the best-fit set-up cases and applied this to all latitudes. Choosing $p_{base} = 4.65$ bar, $r_{cloud} = 0.1$ μm, with 0.05 variance and imaginary refractive index $n_{imag} = 0.001$, $r_{haze} = 0.1$ μm, with 0.3 variance and imag-inary refractive index $n_{imag} = 0.1$, we fitted to the synthetic spectra generated from our fitted Minnaert limb-darkening behaviour for all the latitude bands sampled by the Neptune MUSE observations. The resulting fitted methane deep abundances as a function of latitude are shown in Fig. 6, where we also show the methane abundance variation derived in our previous analysis (Irwin et al., 2019) and that derived by Karkoschka and Tomasko (2011). Here we can see that our derived latitudinal methane distribution (Model 1) varies much more smoothly with latitude, has smaller error bars than our previous analysis (although we must remember that these are random error bars and that there exists in additional $\pm 1\%$ systematic error due to the cloud parameterisation uncertainty) and more closely resembles that determined by Karkoschka and Tomasko (2011). The greatest discrepancy occurs at 20 – 40°S and we found here that our fits had the highest χ^2/n values. To introduce additional flexibility into our model, we ran our retrievals a second time, but additionally allowed the model to vary the imaginary refractive indices of the cloud and haze particles (Model 2), where the ima. It can be seen that Model 2 retrieves lower methane abundances at 20 – 40°S and more closely resembles the results of Karkoschka and Tomasko (2011). Fig. 7 shows the latitudinal variation of n_{imag} retrieved for Model 2 and compares it to the retrieved cloud structure. We can see that n_{imag} for the cloud is poorly constrained, but that of the haze is well constrained. It would appear that to best match the observations at 20 – 40°S the haze particles are required to have slightly lower n_{imag}. This is easily understood looking at Fig. 1 where we can see that this latitude has numerous bright high clouds. Although we masked the observations to bias the retrievals to the background smooth latitudinal variation, to mask completely the brighter clouds at these latitudes would have left us with no data to analyse at all. Hence, we would expect Model 2, which allows the cloud/haze particle reflectivity to vary, to fit the observations more accurately and also retrieve a more reliable latitudinal variation in cloud-top methane abundance.

In addition to providing a better-constrained retrieval of cloud-top methane and one more consistent with HST/STIS determinations (Karkoschka & Tomasko, 2011), we can see that noticeable lower abundance of methane is retrieved near 60°S. This was also reported by Karkoschka and Tomasko (2011). It is difficult to be certain if this is a real feature

as we have much less geometrical coverage of the limb-darkening curves as we approach the south pole, although the errors in the fitted Minnaert $(I/F)_0$ and k parameters should encapsulate this and we can see that the minimum at 65°S is more pronounced tham the error bars there. Hence, this could well be a real feature, which is more easily seen in Fig. 8 which shows the latitudinal variation of methane projected onto the disc of Neptune as seen by VLT/MUSE.

3.4 Discussion

4 Conclusions

In this work, we have done some stuff. The main conclusions of this work can be summarized as follows:

- Derived Minnaert limb-darkening curves and deduced some cool stuff!

References

Borysow, A., Borysow, J., & Fu, Y. (2000, June). Semi-empirical Model of Collision-Induced Absorption Spectra of H_2-H_2 Complexes in the Second Overtone Band of Hydrogen at Temperatures from 50 to 500 K. Icarus, *145*(2), 601-608. doi: 10.1006/icar.2000.6384

Borysow, A., & Frommhold, L. (1989, June). Collision-induced Infrared Spectra of H_2-He Pairs at Temperatures from 18 to 7000 K. II. Overtone and Hot Bands. ApJ, *341*, 549. doi: 10.1086/167515

Borysow, A., Frommhold, L., & Moraldi, M. (1989, January). Collision-induced Infrared Spectra of H_2-He Pairs Involving 0 1 Vibrational Transitions and Temperatures from 18 to 7000 K. ApJ, *336*, 495. doi: 10.1086/167027

Chance, K., & Kurucz, R. L. (2010, June). An improved high-resolution solar reference spectrum for earth's atmosphere measurements in the ultraviolet, visible, and near

infrared. J. Quant. Spec. Radiat. Transf., *111*(9), 1289-1295. doi: 10.1016/j.jqsrt
.2010.01.036

Irwin, P. G. J., Fletcher, L. N., Tice, D., Owen, S. J., Orton, G. S., Teanby, N. A., &
Davis, G. R. (2016, June). Time variability of Neptune's horizontal and vertical cloud
structure revealed by VLT/SINFONI and Gemini/NIFS from 2009 to 2013. Icarus,
271, 418-437. doi: 10.1016/j.icarus.2016.01.015

Irwin, P. G. J., Teanby, N. A., de Kok, R., Fletcher, L. N., Howett, C. J. A., Tsang,
C. C. C., . . . Parrish, P. D. (2008, April). The NEMESIS planetary atmosphere
radiative transfer and retrieval tool. J. Quant. Spec. Radiat. Transf., *109*, 1136-1150.
doi: 10.1016/j.jqsrt.2007.11.006

Irwin, P. G. J., Toledo, D., Braude, A. S., Bacon, R., Weilbacher, P. M., Teanby, N. A.,
. . . Orton, G. S. (2019, October). Latitudinal variation in the abundance of methane
(CH$_4$) above the clouds in Neptune's atmosphere from VLT/MUSE Narrow Field
Mode Observations. Icarus, *331*, 69-82. doi: 10.1016/j.icarus.2019.05.011

Karkoschka, E., & Tomasko, M. (2009, July). The haze and methane distributions on
Uranus from HST-STIS spectroscopy. Icarus, *202*(1), 287-309. doi: 10.1016/j.icarus
.2009.02.010

Karkoschka, E., & Tomasko, M. G. (2010, February). Methane absorption coefficients for
the jovian planets from laboratory, Huygens, and HST data. Icarus, *205*(2), 674-694.
doi: 10.1016/j.icarus.2009.07.044

Karkoschka, E., & Tomasko, M. G. (2011, January). The haze and methane distributions
on Neptune from HST-STIS spectroscopy. Icarus, *211*(1), 780-797. doi: 10.1016/
j.icarus.2010.08.013

Lindal, G. F. (1992, March). The Atmosphere of Neptune: an Analysis of Radio Occultation
Data Acquired with Voyager 2. AJ, *103*, 967. doi: 10.1086/116119

Minnaert, M. (1941). The reciprocity principle in lunar photometry. ApJ, *93*, 403-410. doi:
10.1086/144279

Pérez-Hoyos, S., Sánchez-Lavega, A., Sanz-Requena, J. F., Barrado-Izagirre, N., Carrión-
González, O., Anguiano-Arteaga, A., . . . Braude, A. S. (2020). Color and aerosol
changes in Jupiter after a North Temperate Belt disturbance. Icarus. (submitted)

Plass, G. N., Kattawar, G. W., & Catchings, F. E. (1973, January). Matrix operator
theory of radiative transfer. 1: Rayleigh scattering. Appl. Opt., *12*, 314-329. doi:
10.1364/AO.12.000314